CO$_2$ Pressure-Dependent Microstructure and Morphology of Carbon for Energy Storage: Unraveling the Role of CO$_2$ in Green Synthesis of Carbon Materials

Peng Li [1,2,†], Yun Chen [1,2,†], Chu Liang [1,2,3,*], Chengfu Zeng [2], Xiaoyu (Baohua) Zhang [2], Haichang Zhong [1,*], Wenxian Zhang [1], Xiaohua Zheng [2] and Mingxia Gao [2,3]

1   Fujian Provincial Key Laboratory of Functional Materials and Applications & School of Materials Science and Engineering, Xiamen University of Technology, Xiamen 361024, China
2   Zhejiang Carbon Neutral Innovation Institute & College of Materials Science and Engineering, Zhejiang University of Technology, Hangzhou 310014, China
3   State Key Lab of Silicon Materials & School of Materials Science and Engineering, Zhejiang University, Hangzhou 310027, China
*   Correspondence: cliang@zjut.edu.cn (C.L.); hczhong@xmut.edu.cn (H.Z.)
†   These authors contributed equally to this work.

Abstract: Advanced carbon materials have played an important function in the field of energy conversion and storage. The green and low-carbon synthesis of elemental carbon with controllable morphology and microstructure is the main problem for carbon materials. Herein, we develop a green and low-carbon method to synthesize porous carbon by reacting CO$_2$ with LiAlH$_4$ at low temperatures. The starting reaction temperatures are as low as 142, 121, and 104 °C for LiAlH$_4$ reacting with 1, 30, and 60 bar CO$_2$, respectively. For the elemental carbon, the porosity of elemental carbon gradually decreased, whereas its graphitization degree increased as the CO$_2$ pressure increased from 1 bar to 60 bar. CO$_2$ serves as one of the two reactants and the CO$_2$ pressure can adjust the thermodynamic and kinetic properties of the formation reaction for synthesizing elemental carbon. The mechanism for CO$_2$ pressure-dependent microstructure and morphology of carbon is discussed on the basis of the formation reaction of elemental carbon and gas blowing effect of H$_2$ and CO$_2$. The elemental carbon with different morphology and microstructure exhibits distinct electrochemical lithium storage performance including reversible capacity, rate capability, cycling stability, and Coulombic efficiency, owing to their different lithium storage mechanism. The elemental carbon synthesized at 30 bar CO$_2$ delivers the highest reversible capacity of 506 mAh g^{-1} after 1000 cycles even at 1.0 A g^{-1}. Advanced energy storage technology based on the green and low-carbon synthesis of carbon materials is a requisite for providing a stable and sustainable energy supply to meet the ever-growing demand for energy.

Keywords: green synthesis; elemental carbon; CO$_2$; morphology; lithium storage mechanism

1. Introduction

Carbon materials have been widely applied in the field of energy conversion and storage [1–7]. Energy conversion and storage technologies based on the green and low-carbon synthesis of carbon materials are the necessary premise for achieving carbon neutrality. Carbon materials play a key role in the commercial energy storage devices of lithium-ion batteries (LIBs). Various anode materials, including carbon [8], silicon [9], titanium [10], nitride [11], transition metal oxide [12,13], etc., have been explored. Among them, carbon is regarded as one of the most promising lithium storage materials for the commercial LIBs. Graphite has been widely selected as the commercial anode material for its rich source, low cost and relatively high lithium storage capacity (372 mAh g^{-1}). However, graphite anode material cannot meet the demand of the next generation LIBs with high energy density and high power density [14,15].

Carbon materials are usually synthesized from the organic precursors of biomass [16], polymers [17], and fossil products [18] via a carbonization reaction. The synthesis process involves multiple steps and has the disadvantages of sluggish reaction rate and emission of greenhouse gases and harmful gases [19,20]. Thus, it is crucial to develop a facile, green and low-carbon technology to synthesize carbon materials in the long term. CO_2, as the major contributor of greenhouse effect [21], is also a cheap and easily available precursor for synthesizing carbon materials. High temperature or gaseous pressure may be needed to synthesize elemental carbon from CO_2 because of its high thermodynamic and kinetic stability [22]. CO_2 reacting with magnesium metal and the electrolytic melting carbonate to produce carbon materials both need at least several hours at high temperature [23–27]. The conversion of CO_2 into carbon using cation-excess magnetite is also reported to be required at 290 °C [28,29]. In our previous work, we have achieved green and efficient conversion of CO_2 at low temperatures through various strategies, such as low-temperature heating [30] and mechanochemistry [31]. Moreover, these carbon materials derived from CO_2 show excellent lithium storage performance.

In this work, we report a low-temperature and green method to synthesize elemental carbon with CO_2 pressure dependent morphology and microstructure via reacting CO_2 with $LiAlH_4$. Porous carbon with the specific surface area of 522 $m^2\,g^{-1}$ has been successfully synthesized by reacting CO_2 with $LiAlH_4$ at as low as 142 °C under 1.0 bar CO_2. The function of CO_2 is revealed in the green synthesis of elemental carbon. The mechanism for CO_2 pressure-dependent morphology and microstructure of elemental carbon is studied on the formation reaction for synthesizing elemental carbon and gas-blowing effect of H_2 and CO_2.

2. Experimental Section

2.1. Materials

Lithium aluminium hydride ($LiAlH_4$, 95%), carbon dioxide (CO_2, 99.995%), ethanol (99.7%), and hydrochloric acid (HCl, 37 wt.% in water) were purchased from Alfa Aesar, Jinggong, Ante, and Xilong, respectively. Deionized (DI) water was produced in our lab. All chemicals were used as received.

2.2. Synthesis Procedurer5f4

First, 0.38 g of $LiAlH_4$ were weighted and loaded into a homemade reactor with temperature and gas pressure monitors. These operations were carried out in a glovebox (O_2 < 0.01 ppm, H_2O < 0.01 ppm) filled with argon to prevent $LiAlH_4$ from contacting with water and air. About 1, 30, and 60 bar CO_2 were then introduced into the homemade reactor via a gas injection valve, respectively. The $LiAlH_4$-CO_2 mixture was heated from room temperature to the preset temperature at a rate of 2 °C/min. After reacting $LiAlH_4$ with CO_2, the solid products were collected for washing with excess hydrochloric acid at 200 °C to remove the byproducts. Finally, the suspension of fine particles was collected and washed with DI water and ethanol several times, subsequently dried at 80 °C for 6 h. The elemental carbons synthesized by reacting with 1, 30, and 60 bar CO_2, are referred to as Carbon−1 bar, Carbon−30 bar, and Carbon−60 bar, respectively, in this work.

2.3. Characterization

X-ray diffraction (XRD) patterns of carbon samples were measured in the 2θ range of 10–80° on an X-ray diffractometer (X'Pert Pro diffractometer) with Cu Kα radiation at 40 kV and 40 mA. Raman spectra of carbons were measured on a Renishaw Raman spectrophotometer (Invia plus) with the excitation wavelength of 532 nm. Specific surface area and pore size distribution were analyzed using the Brunauer–Emmett–Teller (BET) model. Field emission scanning electron microscopy (FESEM, Hitachi S-4700) images and high-resolution transmission electron microscopy (HRTEM, FEI Tecnai G^2 F30) images were employed to observe the microstructures and morphologies of electrode materials.

2.4. Electrochemical Measurements

CR2032-typed coin cell was used to evaluate the electrochemical performance of as-synthesized carbons. The working electrode consisted of as-synthesized carbon and polyvinylidene fluoride (PVDF) in a mass ratio of 85:15. The active material (carbon) was mixed with PVDF in the NMP solvent to form a slurry via stirring. The slurries were evenly coated on copper foils and then drying at 80 °C for 20 h in vacuum. Lithium foil (99.9%, China Energy Lithium) was used as the counter electrode, Celgard 2400 membrane as the separator and a solution of 1 M $LiPF_6$ dissolved in ethylene carbonate (EC) and dimethyl carbonate (DMC) in a 1:1 by volume was used as electrolyte. CR2032 coin cells were assembled in an argon-filled glove-box. The electrochemical measurements including galvanostatic discharge/charge test and cyclic voltammetry (CV) measurement were conducted using a Neware battery test system and a CHI650B electrochemical workstation, respectively, in a voltage range of 0.01–3.0 V. All electrochemical performances were tested at room temperature.

3. Results and Discussion

3.1. Synthesis of Elemental Carbon via Reacting CO_2 with $LiAlH_4$

The elemental carbon was synthesized by reacting gaseous CO_2 with solid $LiAlH_4$ in the heating process. Figure 1a shows the time dependence of sample temperatures and gas pressures in the reactor during heating from room temperature to a preset temperature. Three initial CO_2 pressures (1, 30, and 60 bar) were applied to react with $LiAlH_4$ to produce elemental carbon. Abrupt changes in both sample temperatures and gaseous pressures are observed in all the heating process of $LiAlH_4$ reacting with 1, 30, and 60 bar CO_2, implying an exothermic reaction between CO_2 and $LiAlH_4$. The gaseous pressure change is mainly caused by the heat of external heating and internal reaction induced temperature change. As shown in Figure 1a, the starting temperature of the exothermic reaction is found to strongly depend on the initial CO_2 pressure. It is noteworthy that when the sample temperature was elevated to the starting temperature of the exothermic reaction, the external heating was stopped. The starting temperature is found to decrease with increasing the initial CO_2 pressure. The starting temperatures are 142, 121, and 104 °C, respectively, for the $LiAlH_4$ reacting with 1, 30, and 60 bar CO_2. For the exothermic reaction between CO_2 and $LiAlH_4$, the starting temperature increases to the heat of reaction induced maximum temperature in less than 10 s. Interestingly, the maximum temperature increases with increasing the initial CO_2 pressure, in which the maximum temperatures are 165, 330, and 810 °C, respectively, for the $LiAlH_4$ reacting with 1, 30, and 60 bar CO_2.

The elemental carbon was successfully separated from the three abovementioned solid-state products by reacting with hydrochloric acid, confirmed by the energy dispersive X-ray spectroscopies (EDS) as shown in Figure 1d. It can be seen that only element C, O, and a small amount of Al were detected in the three as-synthesized carbon samples. The homogeneity of C, O, and Al can be seen in the elemental distribution mapping of the as-synthesized carbons (Supplementary Figure S1). Taking the Carbon−1 bar as an example, the content of element O is less than 9.74 wt.%, in which the oxygen absorbed may be responsible for the very small amount of element O. Carbon−1 bar exhibits a low graphitization degree as the broad peaks around 25° are seen in the XRD pattern (Figure 1b). As shown in the Raman spectrum of Carbon−1 bar (Figure 1c), the D band centered at 1355 cm^{-1} and G band centered at 1588 cm^{-1} are observed, demonstrating the formation of elemental carbon.
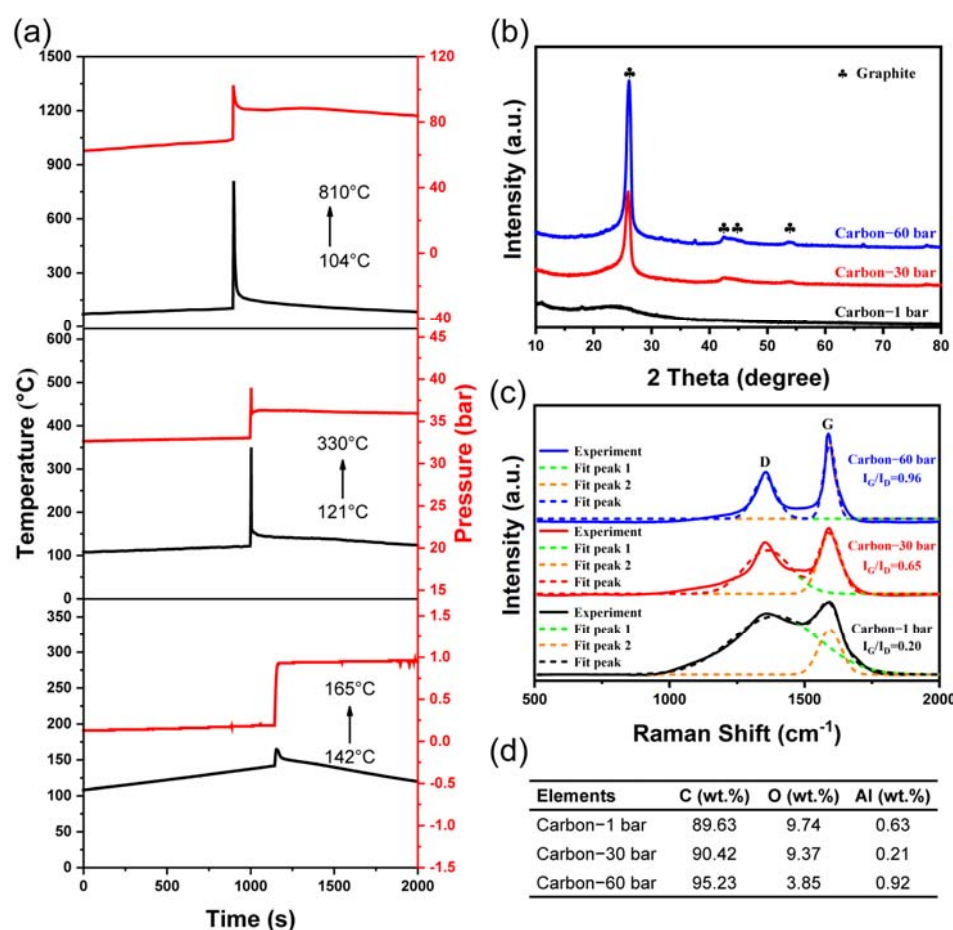
Figure 1. (**a**) Time dependence of sample temperatures and gaseous pressures in the reactor during the synthesis of elemental carbon. (**b**) XRD patterns and (**c**) Raman spectra of Carbon−1 bar, Carbon−30 bar, and Carbon−60 bar. (**d**) Content of elements in the as-obtained carbon.

3.2. Effect of CO_2 Pressure on the Morphology and Microstructure of Elemental Carbon

The XRD patterns of Carbon−1 bar, Carbon−30 bar, and Carbon−60 bar are shown in Figure 1b. Two diffraction peaks centered at 25.9° and 42.4°, assigned to the (002) and (100) planes of hexagonal graphite, are observed in the XRD patterns of both Carbon−30 bar and Carbon−60 bar, which is different from the Carbon−1 bar with low graphitization degree. These results suggest that the graphitization degree of elemental carbon may be related to the CO_2 pressure applied in the synthesis process. The effect of CO_2 pressure on the graphitization degree of elemental carbon was further characterized by Raman spectra (Figure 1c). The area ratio of G band centered at 1588 cm^{-1} to D band centered at 1355 cm^{-1} is used to evaluate the graphitization degree of elemental carbon. The area ratios are 0.20, 0.65, and 0.96, respectively, for Carbon−1 bar, Carbon−30 bar and Carbon−60 bar, implying that the graphitization degree of elemental carbon increases with the CO_2 pressure. The Raman results are consistent with the XRD results.

The porosity of elemental carbon was assessed via N_2 adsorption–desorption isotherms as shown in Figure 2. The BET surface areas are calculated to be 522 m^2 g^{-1} for Carbon−1 bar, 217 m^2 g^{-1} for Carbon−30 bar and 37 m^2 g^{-1} for Carbon−60 bar, respectively, suggesting that the porosity may be distinct for the elemental carbons synthesized under different CO_2 pressures. As shown Figure 2b, three elemental carbons exhibit a continuous mesopore and macro-pore size distribution, in which the pore diameter of elemental carbon increases with the CO_2 pressure applied in its synthesis process.
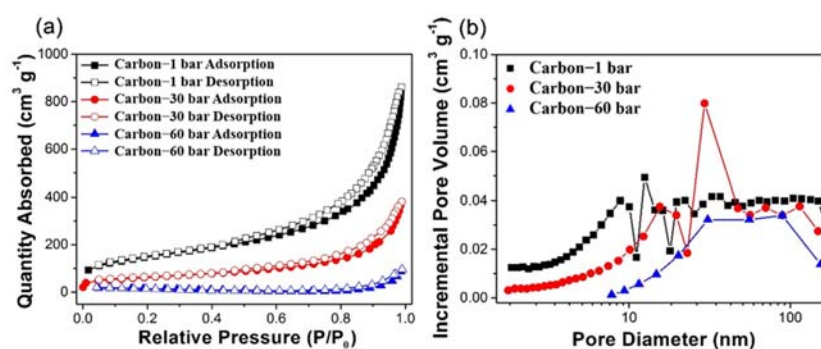
Figure 2. (**a**) Nitrogen adsorption–desorption isotherms and (**b**) the corresponding pore diameter distribution of Carbon−1 bar, Carbon−30 bar, and Carbon−60 bar, respectively.

To verify the effect of CO_2 pressure on the porosity of elemental carbon, the morphology and microstructure of Carbon−1 bar, Carbon−30 bar, and Carbon−60 bar were observed using SEM and TEM (Figure 3). Carbon−1 bar shows a honeycomb morphology with obvious porous structure (Figure 3a,d). When the CO_2 pressure increased to 30 bar, the pore diameter of Carbon−30 bar becomes greater than that of Carbon−1 bar (Figure 3b,e), in good agreement with the BET results. For the Carbon−60 bar, a flaky morphology with unobvious porous structure is observed in the SEM and TEM images (Figure 3c,f). Furthermore, the graphitization degree of three elemental carbons can be characterized using high-resolution TEM (HRTEM) images (Figure 3g–i). For the Carbon−60 bar, distinct lattice fringes with a distance of 0.36 nm can be seen in Figure 3i, corresponding to the (002) plane of graphite [32,33]. As the CO_2 pressure decreased to 30 bar, lattice is defective and graphite plane cannot be calculated accurately (Figure 3h), supporting the decreased graphitization degree compared with Carbon−60 bar. For the Carbon−1 bar (Figure 3g), almost no lattice fringes were detected, resulting from the amorphous nature. The HRTEM results are consistent with the conclusion on graphitization degree drawn from XRD results.
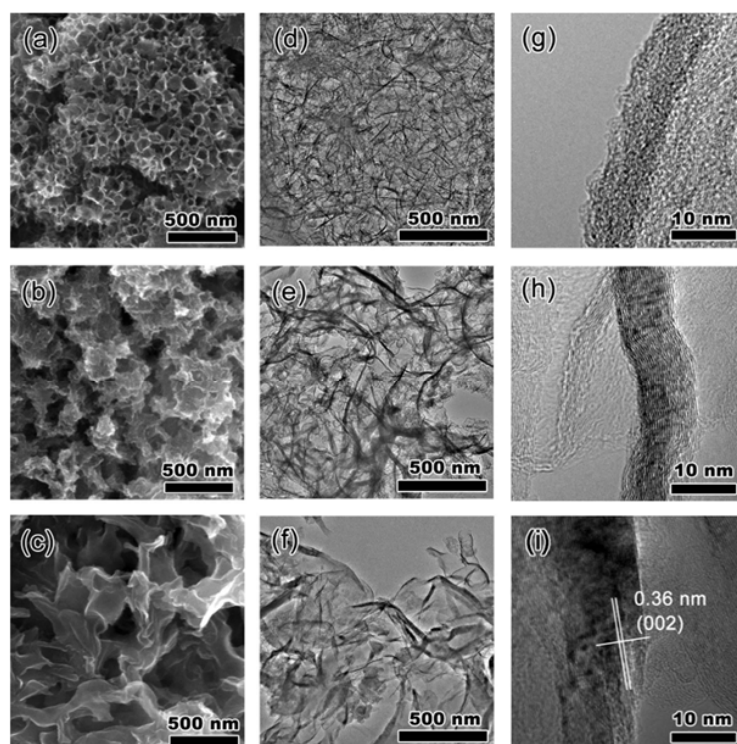

Figure 3. SEM and TEM images and high-resolution TEM images of Carbon−1 bar (**a**,**d**,**g**), Carbon−30 bar (**b**,**e**,**h**), and Carbon−60 bar (**c**,**f**,**i**).

Based on the XRD, BET, TEM, and HRTEM analysis, it has been demonstrated that the morphology and microstructure of elemental carbon synthesized by reacting CO_2 with $LiAlH_4$ is strongly dependent on the CO_2 pressure.

3.3. Mechanism for CO_2 Pressure-Dependent Morphology and Microstructure of Elemental Carbon

Figure 4 exhibits the XRD patterns of the solid products of $LiAlH_4$ reacting with 1, 30, and 60 bar CO_2. $LiAlO_2$, Li_2CO_3, and Al are the main crystal phases in the solid products of $LiAlH_4$ reacting with 1, 30, and 60 bar CO_2, but the relative intensity of three crystal phases is strongly dependent on the CO_2 pressure. As the CO_2 pressure increased from 1 bar to 60 bar, the intensity of $LiAlO_2$ significantly increased, whereas the intensity of Al gradually weakened, as shown in Figure 4, supporting the key role of CO_2 in the chemical interaction of CO_2 with $LiAlH_4$. These results imply that the contents of $LiAlO_2$, Li_2CO_3, and Al phases in the solid products are related to the CO_2 pressure applied in the synthesis process of elemental carbon due to the different thermodynamic properties of the reaction between $LiAlH_4$ and CO_2. According to the abovementioned discussion and our previous work [34], the chemical interaction of CO_2 with $LiAlH_4$ can be described as follows:

$$CO_2 + LiAlH_4 \rightarrow LiAlO_2 + Li_2CO_3 + Al + C \text{ (elemental carbon)} + H_2 \tag{1}$$
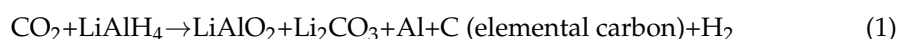
where the equation of chemical reaction of CO_2 with $LiAlH_4$ is not balanced owing to the CO_2 pressure-related phase contents of $LiAlO_2$, Li_2CO_3, and Al in the solid products. The exothermic nature of chemical reaction (1) can be concluded from the reaction characteristics of CO_2 with $LiAlH_4$ as shown in Figure 1a. It should be noted that the morphology and microstructure of elemental carbon synthesized via Equation (1) have been demonstrated to depend on the CO_2 pressure as well.
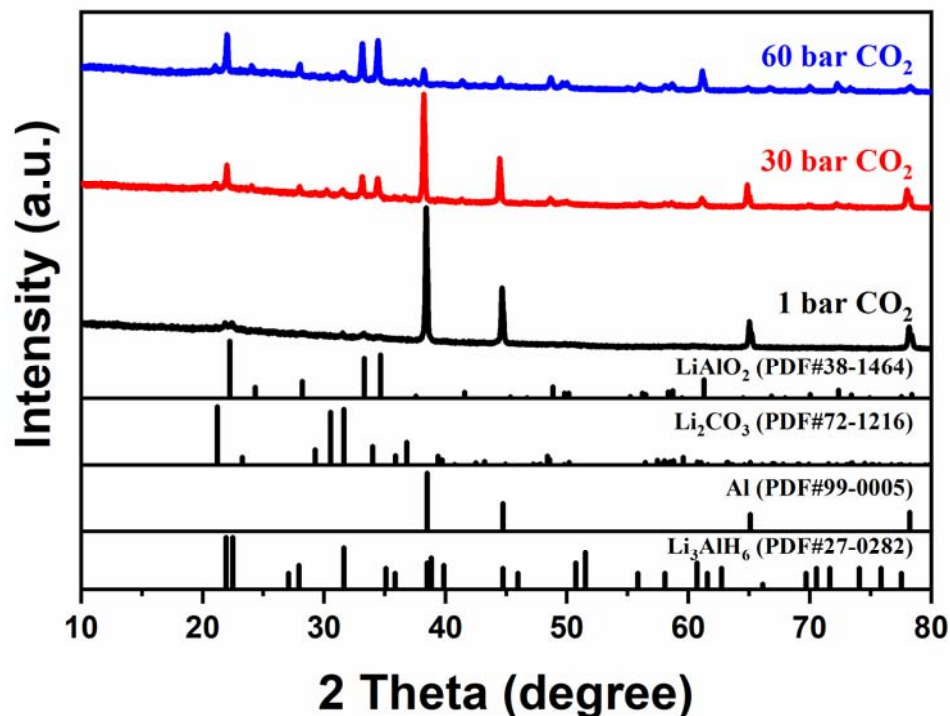

Figure 4. XRD patterns of the solid products of $LiAlH_4$ reacting with 1, 30, and 60 bar CO_2.

CO_2 is one of the two reactants of exothermic reaction (1) in which the thermodynamic and kinetic properties of reaction (1) can be tuned using the CO_2 pressure. It also is the carbon precursor in the green synthesis of elemental carbon (Carbon−1 bar, Carbon−30 bar, and Carbon−60 bar) via the chemical reaction (1). For the exothermic reaction (1), thermodynamic performance is a crucial factor for the reaction heat released during synthesizing

elemental carbon. As shown in Figure 1a, it can be known that the most reaction heat was released in the synthesis process of Carbon−60 bar and the least reaction heat was released in the synthesis process of Carbon−1 bar, according to their difference value between maximum temperature and starting temperature. Moreover, the content of $LiAlO_2$ in the solid products increases with the CO_2 pressure (Figure 4). These results support that more CO_2 was reacted with $LiAlH_4$ to produce more reaction heat under the high CO_2 pressure because the mass of $LiAlH_4$ used in each experiment is a fixed value in this work. As a result, the thermodynamic performance of CO_2 reacting with $LiAlH_4$ can be tuned via the CO_2 pressure. Kinetic performance is the key factor for determining the starting temperature of CO_2 reacting with $LiAlH_4$. The concentration and gaseous pressure of reactants has been demonstrated to be the key factors for the kinetic performance of a gas-solid reaction [35–37]. Compared with Carbon−1 bar, both concentration and gaseous pressure of CO_2 in the synthesis process of Carbon−60 bar are much higher than that of Carbon−1 bar, resulting in the starting reaction temperature decreased with the CO_2 pressure (Figure 1a). The CO_2 pressure-tuned thermodynamic and kinetic performance of chemical reactions for synthesizing elemental carbon may be responsible for the CO_2 pressure-dependent microstructure and morphology of elemental carbon.

For the gas–solid reaction (1), gaseous CO_2 and solid $LiAlH_4$ as reactants are consumed to produce gaseous H_2, solid elemental carbon, and other solid products. Temperature and gaseous pressure are the rate-determining factors of the gas–solid reaction (1). The gaseous H_2 and CO_2 blowing serves the function of adjusting the morphology in the synthesis process of elemental carbons. Gas blowing velocity is found to positively relate to the pore size formed in elemental carbon. No pores were found in the elemental carbon when the gas blowing velocities exceed a certain value. As shown in Figure 1a, a continuous and fast temperature and gaseous pressure distribution, resulting from the exothermic reactions between CO_2 and $LiAlH_4$, is observed in the synthesis process of Carbon−1 bar, Carbon−30 bar, and Carbon−60 bar, supporting the formation of a continuous gas-blowing velocity distribution. Therefore, the elemental carbon with a continuous mesopore and macro-pore size distribution is formed in the synthesis of Carbon−1 bar, Carbon−30 bar, and Carbon−60 bar (Figures 2 and 3). For the Carbon−60 bar, the pore size is greater than that of Carbon−1 bar and Carbon−30 bar due to a higher gas blowing velocity distribution resulted from higher CO_2 pressure and more reaction heat released from CO_2 reacting with $LiAlH_4$. Moreover, the reaction heat and CO_2 pressure are the main factors for tuning the graphitization degree of elemental carbon via the thermodynamic and kinetic performance of reaction (1).

3.4. Electrochemical Properties of Elemental Carbon

The electrochemical lithium storage performance of the three abovementioned elemental carbons were investigated to further confirm the different morphology and microstructure of Carbon−1bar, Carbon−30bar, and Carbon−60bar. Figure 5 displays the discharge/charge and CV curves of Carbon−1 bar, Carbon−30 bar, and Carbon−60 bar. In the first cycle, the elemental carbon anode delivers a discharge/charge capacities of 2415/960 mAh g^{-1} for Carbon−1 bar, 1256/535 mAh g^{-1} for Carbon−30 bar and 711/364 mAh g^{-1} for Carbon−60 bar, corresponding to the initial coulombic efficiency of 39.8, 46.6 and 51.2%, respectively. The irreversible capacity, which can be ascribed to the formation of solid electrolyte interface (SEI)layers on the surface of elemental carbon and the irreversible reaction of lithium ion with functional groups on the surface of elemental carbon [38–40], is found to decrease with the increasing CO_2 pressure, owing to the different specific surface area of Carbon−1 bar, Carbon−30 bar, and Carbon−60 bar. For the Carbon−60 bar, the least SEI layer was formed on its surfaces because of its lowest specific surface area in three elemental carbons. As shown in the CV curves (Figure 5), the lithium storage behaviors of elemental carbon are in good agreement with their galvanostatic discharge/charge results. Three elemental carbon anodes show similar CV curves (Figure 4d–f). In the first cycle, there are two broad cathodic peaks around 0.8 and

1.3 V, corresponding to the formation of SEI layers and the irreversible reactions between elemental carbon anodes and liquid electrolyte. In addition, a sharp peak around 0.01 V was observed for all the three elemental carbon anodes in the following scans. Meanwhile, an anodic peak emerged at around 0.1 V, which can be ascribed to the deintercalation of Li$^+$ cations from the graphite [41–43]. As the graphitization degree of elemental carbon increased from Carbon−1 bar to Carbon−60 bar, the intensity of anodic peak around 0.1 V become more and more sharp and manifest.
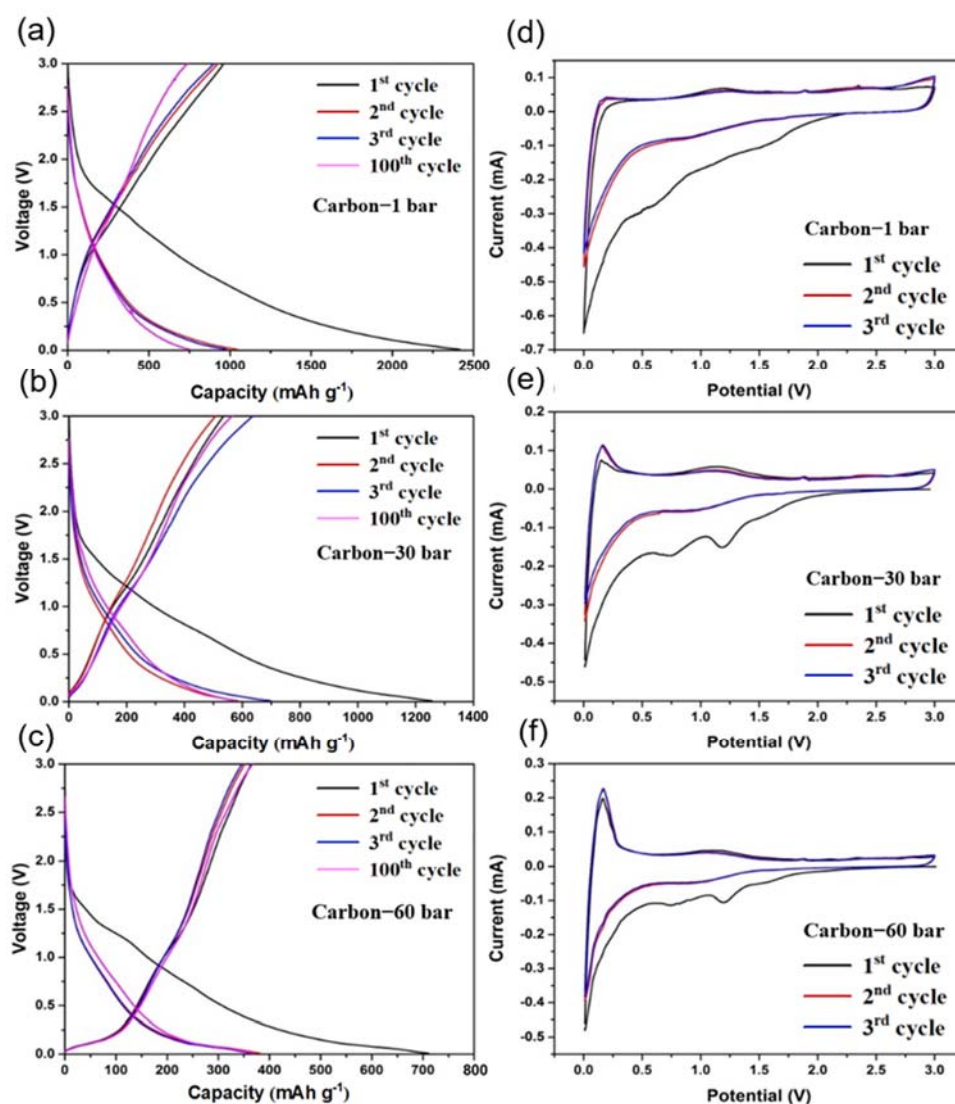

Figure 5. The galvanostatic charge/discharge profiles (**a**–**c**) at a current density of 100 mA g^{-1} and CV curves (**d**–**f**) of the elemental carbon anodes in a voltage range of 0.01–3.0 V.

Figure 6a presents the cycling properties of the Carbon−1 bar, Carbon−30 bar, and Carbon−60 bar at a current density of 100 mA g^{-1}. It can be clearly seen that the electrochemical performance of elemental carbon, including lithium storage capacity, Coulombic efficiency and cycling stability, is found to be related to the CO_2 pressure applied in the synthesis of elemental carbon. For Carbon−1 bar and Carbon−30 bar, the capacity deterioration is only observed in the first 10 cycles. On the contrary, Carbon−60 bar exhibits a good cycling stability with the minimum reversible capacities of ~370 mAh g^{-1} over 100 cycles. Carbon−1 bar delivers the highest reversible lithium storage capacity of 738 mAh g^{-1} over 100 cycles. The corresponding reversible capacity is ~570 mAh g^{-1} for Carbon−30 bar.
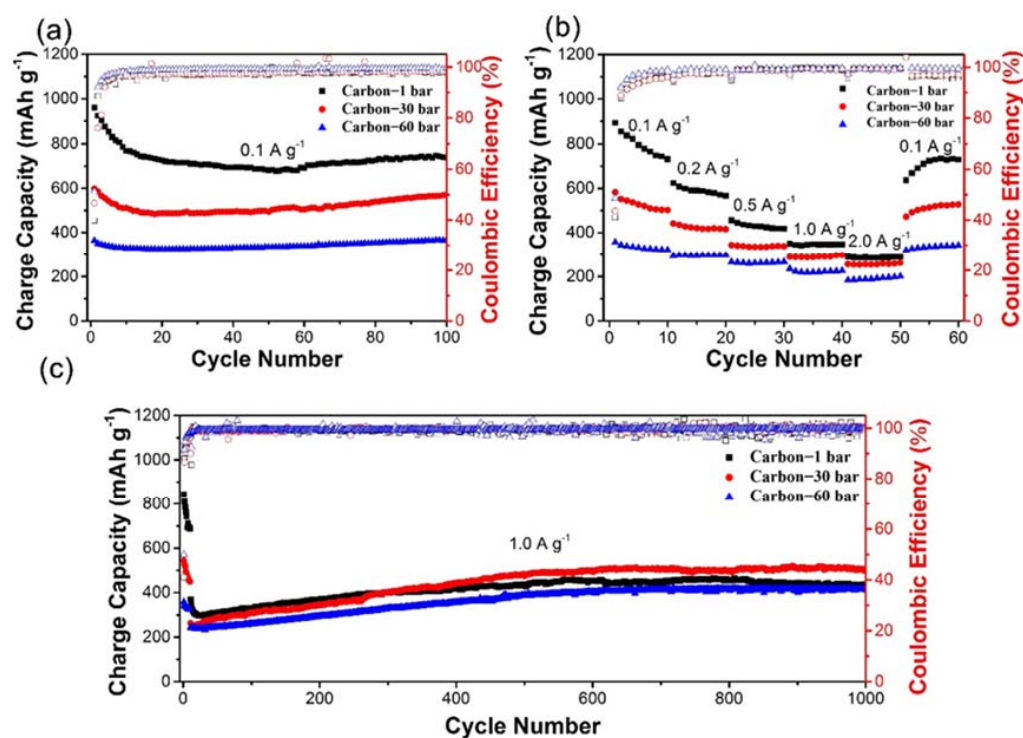
Figure 6. Electrochemical performance of Carbon−1 bar, Carbon−30 bar, and Carbon−60 bar. (**a**) Cycling properties and Coulombic efficiency at a current density of 100 mA g^{-1}, (**b**) rate performance and (**c**) ultra-long cycling performance at a current density of 1000 mA g^{-1}.

The rate capability of Carbon−1 bar, Carbon−30 bar, and Carbon−60 bar was tested at the current densities of 0.1, 0.2, 0.5, 1.0 and 2.0 A g^{-1} (Figure 6b). The Carbon−1 bar exhibits the maximum reversible lithium storage capacity at all the current densities. The charge capacity of the Carbon−1 bar is 795, 589, 430, 348, and 285 mAh g^{-1}, respectively, at 0.1, 0.2, 0.5, 1.0, and 2.0 A g^{-1}. However, the Carbon−1 bar has the lowest capacity retention, compared with Carbon−30 bar and Carbon−60 bar. Carbon−60 bar exhibits the highest capacity retention, in which the capacity retention is about 92%, 83%, 71%, and 62%, respectively, at the current densities of 0.2, 0.5, 1.0, and 2.0 A g^{-1}. To evaluate the electrochemical stability of obtained carbon derived from CO_2, long-term cycling performance of Carbon−1 bar, Carbon−30 bar, and Carbon−60 bar was measured at a current density of 100 mA g^{-1} for first 10 cycles, and then at 1.0 A g^{-1} for the following 1000 cycles (Figure 6c). At the current density of 1.0 A g^{-1}, elemental carbon reaches the minimum capacity of 299 mAh g^{-1} for Carbon−1 bar after 10 cycles, 246 mAh g^{-1} for Carbon−30 bar after 2 cycles, and 242 mAh g^{-1} for Carbon−60 bar after 1 cycle. It can be seen that the charge capacity measured at 1.0 A g^{-1} increases gradually from a minimum value to a stable value at 500th cycle during repeated cycling. The increase rate is found to be related to the CO_2 pressure applied in the synthesis of elemental carbon. Carbon−30 bar exhibits the highest increase rate as shown in Figure 6c. After 500 cycles, they deliver stable reversible capacities of 443 mAh g^{-1} for Carbon−1 bar, 486 mAh g^{-1} for Carbon−30 bar and 390 mAh g^{-1} for Carbon−60 bar, respectively. After 1000 cycles, Carbon−30 bar delivers the highest reversible capacity of 506 mAh g^{-1} at 1.0 A g^{-1}. Compared with the recent work on carbon materials [44–47], the elemental carbons synthesized from CO_2 in this work show higher lithium storage capacity and longer cycle life. Moreover, the electrochemical properties of the elemental carbon can be tuned by CO_2 pressure in the synthesis process, in order to match different application scenarios.

As discussed above, it is known that the electrochemical performance is dependent on the CO_2 pressure applied in the synthesis of elemental carbon. For Carbon−1 bar, Carbon−30 bar, and Carbon−60 bar, the difference in electrochemical performance includ-

ing lithium storage capacity, rate capability, and cycling stability can be ascribed to their different microstructures and morphologies, resulting from the distinct lithium storage mechanisms. As shown in Figure 5, Carbon−1 bar and Carbon−30 bar exhibit remarkable capacitance-dominated lithium storage behaviors, but a very small proportion of the graphite-dominated lithium storage behaviors is observed in the Carbon−30 bar. For the Carbon−60 bar, the remarkable graphite-dominated and capacitance-dominated lithium storage behaviors are observed in Figure 5c,f. The capacitance-dominated lithium storage mechanism is responsible for the high lithium storage capacity and the superior rate capability due to more lithium storage sites on the surfaces and in the interfaces of elemental carbon with porous structure. In contrast, the graphite-dominated lithium storage mechanism is responsible for relatively low lithium storage capacity and the high Coulombic efficiency, especially for the initial efficiency, and the excellent cycling stability. As predicted, Carbon−1bar, Carbon−30 bar, and Carbon−60 bar exhibit the distinct electrochemical lithium storage properties, supporting that the CO_2 pressure-tuned microstructure and morphology of elemental carbons.

4. Conclusions

In summary, we have demonstrated a green and low-carbon method to synthesize carbon materials with controllable morphology and microstructure from CO_2 by reacting $LiAlH_4$ with different CO_2 pressure. As the CO_2 pressure increased from 1 bar to 30 and 60 bar, the starting reaction temperature decreased from 142 °C to 121 and 104 °C, resulting in CO_2 pressure-dependent morphology and microstructure of carbon materials. As an example, the BET surface areas are 522 m^2 g^{-1} for Carbon−1 bar, 217 m^2 g^{-1} for Carbon−30 bar and 37 m^2 g^{-1} for Carbon−60 bar, respectively. CO_2 can react with $LiAlH_4$ to produce $LiAlO_2$, Li_2CO_3, Al, C (elemental carbon), and H_2 in the synthesis of carbon materials. The reaction temperature and products, which are the key factors for determining morphology and microstructure of carbon materials, are demonstrated to be strongly associated with CO_2 pressure. More CO_2 was reacted with $LiAlH_4$ to produce more reaction heat under the high CO_2. The CO_2 pressure-tuned thermodynamic and kinetic performance of chemical reactions for synthesizing elemental carbon is responsible for the CO_2 pressure-dependent microstructure and morphology of elemental carbon. The elemental carbon exhibits CO_2 pressure-related electrochemical performance. Carbon−1 bar delivers a high reversible capacity of 738 mAh g^{-1} in the current density of 100 mA g^{-1} after 100 cycles. Carbon−30 bar shows a high-rate capability of 506 mAh g^{-1} even at 1 A g^{-1} over 1000 cycles. Carbon−60 bar exhibits high capacity retention at various current densities. The difference in electrochemical performance can be ascribed to their different microstructures and morphologies, resulting from the distinct lithium storage mechanisms.

Conflicts of Interest: The authors declare no conflict of interest.

References

1. Luo, Q.; Liu, P.; Fu, L.; Hu, Y.; Yang, L.; Wu, W.; Kong, X.Y.; Jiang, L.; Wen, L. Engineered Cellulose Nanofiber Membranes with Ultrathin Low-Dimensional Carbon Material Layers for Photothermal-Enhanced Osmotic Energy Conversion. *ACS Appl. Mater. Interfaces* **2022**, *14*, 13223–13230. [CrossRef] [PubMed]
2. Moyer, K.; Meng, C.; Marshall, B.; Assal, O.; Eaves, J.; Perez, D.; Karkkainen, R.; Roberson, L.; Pint, C.L. Carbon fiber reinforced structural lithium-ion battery composite: Multifunctional power integration for CubeSats. *Energy Storage Mater.* **2020**, *24*, 676–681. [CrossRef]
3. Tang, Z.; Gao, Y.; Cheng, P.; Jiang, Y.; Xu, J.; Chen, X.; Li, A.; Wang, G. Metal-organic framework derived magnetic phase change nanocage for fast-charging solar-thermal energy conversion. *Nano Energy* **2022**, *99*, 107383. [CrossRef]
4. Wang, X.; Yang, C.; Li, J.; Chen, X.A.; Yang, K.; Yu, X.; Lin, D.; Zhang, Q.; Wang, S.; Wang, J.; et al. Insights of Heteroatoms Doping-Enhanced Bifunctionalities on Carbon Based Energy Storage and Conversion. *Adv. Funct. Mater.* **2020**, *31*, 2009109. [CrossRef]
5. Yang, S.; Cheng, Y.; Xiao, X.; Pang, H. Development and application of carbon fiber in batteries. *Chem. Eng. J.* **2020**, *384*, 123294. [CrossRef]
6. Zhang, W.; Yin, J.; Chen, C.; Qiu, X. Carbon nitride derived nitrogen-doped carbon nanosheets for high-rate lithium-ion storage. *Chem. Eng. Sci.* **2021**, *241*, 116709. [CrossRef]
7. Zhao, C.; Li, H.; Zou, Y.; Qi, Y.; Jian, Z.; Chen, W. Low-cost carbon materials as anode for high-performance potassium-ion batteries. *Mater. Lett.* **2020**, *262*, 127147. [CrossRef]
8. Naraprawatphong, R.; Chokradjaroen, C.; Thiangtham, S.; Yang, L.; Saito, N. Nanoscale advanced carbons as an anode for lithium-ion battery. *Mater. Today Adv.* **2022**, *16*, 100290. [CrossRef]
9. Ma, Y.; Qu, H.; Wang, W.; Yu, Y.; Zhang, X.; Li, B.; Wang, L. Si/SiO$_2$@Graphene Superstructures for High-Performance Lithium-Ion Batteries. *Adv. Funct. Mater.* **2022**, 2211648. [CrossRef]
10. Santhoshkumar, P.; Subburaj, T.; Kathalingam, A.; Karuppasamy, K.; Vikraman, D.; Yim, C.-J.; Park, H.-C.; Kim, H.-S. Potential core-shell anode material for rechargeable lithium-ion batteries: Encapsulation of titanium oxide nanostructure in conductive polymer. *J. Alloys Compd.* **2021**, *882*, 160715. [CrossRef]
11. Pandel, D.; Neises, J.; Kilian, S.O.; Wiggers, H.; Benson, N. Lithium-Ion Battery Anodes Based on Silicon Nitride Nanoparticles as Active Material and Vertically Aligned Carbon Nanotubes as Electrically Conductive Scaffolding. *ACS Appl. Energy Mater.* **2022**, *5*, 14807–14814. [CrossRef]
12. Liang, Z.; Tu, H.; Kong, Z.; Yao, X.; Xu, D.; Liu, S.; Shao, Y.; Wu, Y.; Hao, X. Urchin like inverse spinel manganese doped NiCo$_2$O$_4$ microspheres as high performances anode for lithium-ion batteries. *J. Colloid Interface Sci.* **2022**, *616*, 509–519. [CrossRef] [PubMed]
13. Tang, F.; Sun, Y.-G.; Dai, G.-X.; Yan, J.-L.; Lin, X.-J.; Qiu, J.-H.; Cao, A.-M. Template-free synthesis of Co-based oxides nanotubes as potential anodes for lithium-ion batteries. *J. Alloys Compd.* **2022**, *895*, 162611. [CrossRef]
14. Fan, Z.J.; Yan, J.; Wei, T.; Ning, G.Q.; Zhi, L.J.; Liu, J.C.; Cao, D.X.; Wang, G.L.; Wei, F. Nanographene-Constructed Carbon Nanofibers Grown on Graphene Sheets by Chemical Vapor Deposition: High-Performance Anode Materials for Lithium Ion Batteries. *ACS Nano* **2011**, *5*, 2787–2794. [CrossRef]
15. Yi, J.; Li, X.P.; Hu, S.J.; Li, W.S.; Zhou, L.; Xu, M.Q.; Lei, J.F.; Hao, L.S. Preparation of hierarchical porous carbon and its rate performance as anode of lithium ion battery. *J. Power Sources* **2011**, *196*, 6670–6675. [CrossRef]
16. Destyorini, F.; Amalia, W.C.; Irmawati, Y.; Hardiansyah, A.; Priyono, S.; Aulia, F.; Oktaviano, H.S.; Hsu, Y.-I.; Yudianti, R.; Uyama, H. High Graphitic Carbon Derived from Coconut Coir Waste by Promoting Potassium Hydroxide in the Catalytic Graphitization Process for Lithium-Ion Battery Anodes. *Energy Fuels* **2022**, *36*, 5444–5455. [CrossRef]
17. Ehi-Eromosele, C.O.; Onwucha, C.N.; Ajayi, S.O.; Melinte, G.; Hansen, A.-L.; Indris, S.; Ehrenberg, H. Ionothermal synthesis of activated carbon from waste PET bottles as anode materials for lithium-ion batteries. *RSC Adv.* **2022**, *12*, 34670–34684. [CrossRef]
18. Thapaliya, B.P.; Luo, H.; Li, M.; Tsai, W.-Y.; Meyer, H.M.; Dunlap, J.R.; Nanda, J.; Belharouak, I.; Dai, S. Molten Salt Assisted Low-Temperature Electro-Catalytic Graphitization of Coal Chars. *J. Electrochem. Soc.* **2021**, *168*, 046504. [CrossRef]
19. Wang, Z.; Xing, B.; Zeng, H.; Huang, G.; Liu, X.; Guo, H.; Zhang, C.; Cao, Y.; Chen, Z. Space-confined carbonization strategy for synthesis of carbon nanosheets from glucose and coal tar pitch for high-performance lithium-ion batteries. *Appl. Surf. Sci.* **2021**, *547*, 149228. [CrossRef]
20. Xu, H.; Yin, C.; Hou, X.; Gong, M.; Yang, C.; Xu, L.; Luo, J.; Ma, L.; Zhou, L.; Li, X. Polyimide-derived carbon nanofiber membranes as free-standing anodes for lithium-ion batteries. *RSC Adv.* **2022**, *12*, 21904–21915. [CrossRef]
21. Müller, L.J.; Kätelhön, A.; Bringezu, S.; McCoy, S.; Suh, S.; Edwards, R.; Sick, V.; Kaiser, S.; Cuéllar-Franca, R.; El Khamlichi, A.; et al. The carbon footprint of the carbon feedstock CO$_2$. *Energy Environ. Sci.* **2020**, *13*, 2979–2992. [CrossRef]
22. Das Neves Gomes, C.; Blondiaux, E.; Thuery, P.; Cantat, T. Metal-free reduction of CO$_2$ with hydroboranes: Two efficient pathways at play for the reduction of CO$_2$ to methanol. *Chem. Eur. J.* **2014**, *20*, 7098–7106. [CrossRef] [PubMed]
23. Chen, X.; Zhao, Z.; Qu, J.; Zhang, B.; Ding, X.; Geng, Y.; Xie, H.; Wang, D.; Yin, H. Electrolysis of Lithium-Free Molten Carbonates. *ACS Sustain. Chem. Eng.* **2021**, *9*, 4167–4174. [CrossRef]
24. Dong, H.; Guo, S.; Zhao, L. Facile Preparation of Multilayered Graphene with CO$_2$ as a Carbon Source. *Appl. Sci.* **2019**, *9*, 4482. [CrossRef]

25. Wang, X.; Sharif, F.; Liu, X.; Licht, G.; Lefler, M.; Licht, S. Magnetic carbon nanotubes: Carbide nucleated electrochemical growth of ferromagnetic CNTs from CO_2. *J. CO_2 Util.* **2020**, *40*, 101218. [CrossRef]

26. Yu, R.; Xiang, J.; Du, K.; Deng, B.; Chen, D.; Yin, H.; Liu, Z.; Wang, D. Electrochemical Growth of High-Strength Carbon Nanocoils in Molten Carbonates. *Nano Lett.* **2022**, *22*, 97–104. [CrossRef]

27. Zhang, Y.; Du, N.; Chen, Y.; Lin, Y.; Jiang, J.; He, Y.; Lei, Y.; Yang, D. Carbon dioxide as a green carbon source for the synthesis of carbon cages encapsulating porous silicon as high performance lithium-ion battery anodes. *Nanoscale* **2018**, *10*, 5626–5633. [CrossRef]

28. Chun-lei, Z.; Zhi-qiang, L.; Tong-hao, W.; Hong-mao, Y.; Hong-mao, Y. Complete reduction of carbon dioxide to carbon and indirect conversion to O_2 using cation-excess magnetite. *Mater. Chem. Phys.* **1996**, *44*, 194–198. [CrossRef]

29. Tamaura, Y.; Tabata, M. Complete reduction of carbon dioxide to carbon using cation-excess magnetite. *Nature* **1990**, *346*, 255–256. [CrossRef]

30. Wang, K.; Feng, G.; Liang, C.; Xia, Y.; Zhang, J.; Gan, Y.; Huang, H.; Tao, X.; Zhang, W. Green and Low-Temperature Synthesis of Foam-like Hierarchical Porous Carbon from CO_2 as Superior Lithium Storage Material. *ACS Appl. Energy Mater.* **2018**, *1*, 7123–7129. [CrossRef]

31. Liang, C.; Pan, L.; Liang, S.; Xia, Y.; Liang, Z.; Gan, Y.; Huang, H.; Zhang, J.; Zhang, W. Ultraefficient Conversion of CO_2 into Morphology-Controlled Nanocarbons: A Sustainable Strategy toward Greenhouse Gas Utilization. *Small* **2019**, *15*, 1902249. [CrossRef] [PubMed]

32. Lee, H.J.; Cho, W.; Lim, E.; Oh, M. One-pot synthesis of magnetic particle-embedded porous carbon composites from metal–organic frameworks and their sorption properties. *Chem. Commun.* **2014**, *50*, 5476. [CrossRef] [PubMed]

33. Yao, Y.; Fu, K.K.; Zhu, S.; Dai, J.; Wang, Y.; Pastel, G.; Chen, Y.; Li, T.; Wang, C.; Li, T.; et al. Carbon Welding by Ultrafast Joule Heating. *Nano Lett.* **2016**, *16*, 7282–7289. [CrossRef] [PubMed]

34. Liang, C.; Chen, Y.; Wu, M.; Wang, K.; Zhang, W.; Gan, Y.; Huang, H.; Chen, J.; Xia, Y.; Zhang, J.; et al. Green synthesis of graphite from CO_2 without graphitization process of amorphous carbon. *Nat. Commun.* **2021**, *12*, 119. [CrossRef]

35. Sohn, H.Y.; Aboukheshem, M.B. Gas-Solid Reaction-Rate Enhancement by Pressure Cycling. *Metall. Trans. B* **1992**, *23B*, 285. [CrossRef]

36. Muhich, C.L.; Weston, K.C.; Arifin, D.; McDaniel, A.H.; Musgrave, C.B.; Weimer, A.W. Extracting Kinetic Information from Complex Gas–Solid Reaction Data. *Ind. Eng. Chem. Res.* **2014**, *54*, 4113–4122. [CrossRef]

37. Setoodeh Jahromy, S.; Birkelbach, F.; Jordan, C.; Huber, C.; Harasek, M.; Werner, A.; Winter, F. Impact of Partial Pressure, Conversion, and Temperature on the Oxidation Reaction Kinetics of Cu_2O to CuO in Thermochemical Energy Storage. *Energies* **2019**, *12*, 508. [CrossRef]

38. Huang, J.; Lin, Y.; Ji, M.; Cong, G.; Liu, H.; Yu, J.; Yang, B.; Li, C.; Zhu, C.; Xu, J. Nitrogen-doped porous carbon derived from foam polystyrene as an anode material for lithium-ion batteries. *Appl. Surf. Sci.* **2020**, *504*, 144398. [CrossRef]

39. Yan, C.; Zhao, H.; Li, J.; Jin, H.; Liu, L.; Wu, W.; Wang, J.; Lei, Y.; Wang, S. Mild-Temperature Solution-Assisted Encapsulation of Phosphorus into ZIF-8 Derived Porous Carbon as Lithium-Ion Battery Anode. *Small* **2020**, *16*, 1907141. [CrossRef]

40. Issatayev, N.; Kalimuldina, G.; Nurpeissova, A.; Bakenov, Z. Biomass-Derived Porous Carbon from Agar as an Anode Material for Lithium-Ion Batteries. *Nanomaterials* **2022**, *12*, 22. [CrossRef]

41. Yang, S.; Feng, X.; Zhi, L.; Cao, Q.; Maier, J.; Müllen, K. Nanographene-Constructed Hollow Carbon Spheres and Their Favorable Electroactivity with Respect to Lithium Storage. *Adv. Mater.* **2010**, *22*, 838–842. [CrossRef] [PubMed]

42. Han, F.-D.; Bai, Y.-J.; Liu, R.; Yao, B.; Qi, Y.-X.; Lun, N.; Zhang, J.-X. Template-Free Synthesis of Interconnected Hollow Carbon Nanospheres for High-Performance Anode Material in Lithium-Ion Batteries. *Adv. Energy Mater.* **2011**, *1*, 798–801. [CrossRef]

43. Tang, J.; Deng, B.; Xu, F.; Xiao, W.; Wang, D. The lithium storage performance of electrolytic-carbon from CO_2. *J. Power Sources* **2017**, *341*, 419–426. [CrossRef]

44. Chen, X.; Zhao, Z.; Zhou, Y.; Shu, Y.; Sajjad, M.; Bi, Q.; Ren, Y.; Wang, X.; Zhou, X.; Liu, Z. MWCNTs modified α-Fe_2O_3 nanoparticles as anode active materials and carbon nanofiber paper as a flexible current collector for lithium-ion batteries application. *J. Alloys Compd.* **2019**, *776*, 974–983. [CrossRef]

45. Tai, Z.; Shi, M.; Chong, S.; Chen, Y.; Shu, C.; Dai, X.; Tan, Q.; Liu, Y. N-doped ZIF-8-derived carbon (NC-ZIF) as an anodic material for lithium-ion batteries. *J. Alloys Compd.* **2019**, *800*, 1–7. [CrossRef]

46. Drews, M.; Büttner, J.; Bauer, M.; Ahmed, J.; Sahu, R.; Scheu, C.; Vierrath, S.; Fischer, A.; Biro, D. Spruce Hard Carbon Anodes for Lithium-Ion Batteries. *ChemElectroChem* **2021**, *8*, 4750–4761. [CrossRef]

47. Gu, Y.; Tang, Y.; Liu, L.; Zhang, Y.; Gao, Y.; Zhang, Y.; Yang, C.; Liu, T. Semi-coke-based amorphous porous carbon synthesized by a molten salt assisted method for superior lithium storage. *New J. Chem.* **2023**, *47*, 2907–2913. [CrossRef]